Peritumoral tissue compression is predictive of exudate flux in a rat model of cerebral tumor: an MRI study in an embedded tumor

James R. Ewing[a,b,c]*, Tavarekere N. Nagaraja[d], Madhava P. Aryal[e], Kelly A. Keenan[d], Rasha Elmghirbi[a,c], Hassan Bagher-Ebadian[a,c], Swayamprava Panda[a], Mei Lu[f], Tom Mikkelsen[a,d], Glauber Cabral[a] and Stephen L. Brown[g]

MRI estimates of extracellular volume and tumor exudate flux in peritumoral tissue are demonstrated in an experimental model of cerebral tumor. Peritumoral extracellular volume predicted the tumor exudate flux.

Eighteen RNU athymic rats were inoculated intracerebrally with U251MG tumor cells and studied with dynamic contrast enhanced MRI (DCE-MRI) approximately 18 days post implantation. Using a model selection paradigm and a novel application of Patlak and Logan plots to DCE-MRI data, the distribution volume (i.e. tissue porosity) in the leaky rim of the tumor and that in the tissue external to the rim (the outer rim) were estimated, as was the tumor exudate flow from the inner rim of the tumor through the outer rim.

Distribution volume in the outer rim was approximately half that of the inner adjacent region ($p < 1 \times 10^{-4}$). The distribution volume of the outer ring was significantly correlated ($R^2 = 0.9$) with tumor exudate flow from the inner rim. Thus, peritumoral extracellular volume predicted the rate of tumor exudate flux. One explanation for these data is that perfusion, i.e. the *delivery* of blood to the tumor, was regulated by the compression of the mostly normal tissue of the tumor rim, and that the tumor exudate flow was limited by tumor perfusion. Copyright © 2015 John Wiley & Sons, Ltd.

Additional supporting information may be found in the online version of this article at the publisher's web site.

Keywords: tumor interstitial volume; interstitial flow; Logan plot; Patlak plot; dynamic contrast enhanced MRI; DCE-MRI; tumor vasculature

INTRODUCTION

Using animals implanted with a model U251 cerebral tumor and studied twice in a 24 h interval by dynamic contrast enhanced MRI (DCE-MRI), an estimate of tissue extracellular volume fractions in both tumor boundary and the surrounding normal tissue will be presented. The outward flux of a contrast agent (CA) in interstitial tumor exudate in the tumor boundary will also be presented. Extracellular volume fraction and flux in the tumor boundary will be shown to be highly correlated.

An outward transport of CA may indicate increased tumor interstitial fluid pressure (TIFP) (1–4), which is associated with increased tumor aggressiveness (3). In order to non-invasively quantify TIFP, both the velocity of tumor fluid exudate and tissue fluid conductivity in the tumor boundary must be measured. It is the purpose of this paper to demonstrate methods for quantifying the extracellular distribution volume (V_D) of CA at the tumor edge and in its normal surroundings, and to estimate tumor exudate flux at the tumor boundary. V_D is closely related to

* Correspondence to: J. R. Ewing, Department of Neurology, Henry Ford Hospital, Detroit, MI, USA.
E-mail: jewing1@hfhs.org

a J. R. Ewing, R. Elmghirbi, H. Bagher-Ebadian, S. Panda, T. Mikkelsen, G. Cabral
   Department of Neurology, Henry Ford Hospital, Detroit, MI, USA

b J. R. Ewing
   Department of Neurology, Wayne State University, Detroit, MI, USA

c J. R. Ewing, R. Elmghirbi, H. Bagher-Ebadian
   Department of Physics, Oakland University, Rochester, MI, USA

d T. N. Nagaraja, K. A. Keenan, T. Mikkelsen
   Department of Neurosurgery, Henry Ford Hospital, Detroit, MI, USA

e M. P. Aryal
   Department of Radiation Oncology, University of Michigan Medical School, Ann Arbor, MI, USA

f M. Lu
   Department of Public Health Sciences, Henry Ford Hospital, Detroit, MI, USA

g S. L. Brown
   Department of Radiation Oncology, Henry Ford Hospital, Detroit, MI, USA

Abbreviations used: *DCE-MRI, dynamic contrast enhanced MRI; CA, contrast agent; v_p, plasma volume; AIF, arterial input function; K^{trans}, forward volume transfer constant; v_e, interstitial volume fraction; V_D, extracellular distribution volume; k_{ep}, reverse transfer constant; ROI, region of interest; SM, standard model; GLM, generalized linear model; AIC, Akaike information criterion; 2GE, dual-echo gradient-echo; LL, Look–Locker; TIFP, tumor interstitial fluid pressure; PET, positron emission tomography; H&E, hematoxylin and eosin.*

porosity (φ), which in turn may be used, with appropriate calibration, to estimate tissue fluid conductivity (5).

The stepping-off point of this paper lies in a previous consideration of model selection and systematic errors in DCE-MRI studies (6), where it was shown (Fig. 7 of Reference 6) in the rat model of cerebral tumor employed herein that, in the apparently normal tissue rimming the embedded tumor, model failure in the form of near-zero and even negative estimates of plasma volume (v_p) typically occurred. The apparent cause of this model failure (Figs 1–3 of Reference 6) was the transport, via tumor exudate streaming, of the CA from the tumor interior to the voxels where the negative estimates of v_p appeared.

Herein, a Logan plot (7–9) is used to estimate the V_D of CA in the tumor itself, and, uniquely, in the tumor surroundings. We have found (9) that a Logan plot estimate of V_D in the tumor is well correlated with cellular density and with a standard model (SM) (10) estimate of an equivalent quantity. Assuming that the border of the leaky vasculature can be identified and associated with the tumor, it will be demonstrated that a stable estimate of V_D in the tumor surround can be generated by a Logan plot with an appropriately chosen input function. With the same assumptions it will also be shown that a Patlak plot can estimate exudate flux through the tumor rim. Finally, the association of V_D and flux at the tumor periphery will be demonstrated.

METHODS

Experimental methods, including the animal model, sample size, imaging methods and post-mortem histopathology have been previously described (9,11) and are further summarized in the supplementary material. All the animals presented herein have had their test–retest DCE-MRI studies analyzed for standard pharmacokinetic parameters, with results summarized and reported in Reference 11. Thus, the experimental methods used herein will be only briefly summarized.

In a protocol approved by the Henry Ford Hospital Institutional Animal Care and Use Committee, 18 RNU athymic rats were inoculated intracerebrally with U251MG tumor cells and imaged approximately 18 days post-implantation. Tumors when imaged were about 5 mm in diameter. In order to establish test–retest variation in this animal model, two MRI studies were conducted for each animal, 24 h apart.

DCE-MRI studies were performed at 7 T. The DCE-MRI sequence used was a dual-echo spoiled gradient-recalled (2GE) sequence with a 60 ms T_R and tip-angle of 27°. This allowed the direct calculation of changes in T_2^* after the injection of CA, and thus the construction of a time trace of change in R_1 that was free from T_2^* dephasing effects. Details may be found in Reference 6. A three-slice set of 2 mm slices was centered over the tumor and a total of 150 image sets at intervals of 4 s were taken. Total run time was 10 min. Prior to the 2GE sequence, and immediately afterwards, two Look–Locker (LL) sequences were run so that a voxel-by-voxel estimate of T_1 in the tissue could be made pre and post CA administration. CA (Magnevist, Bayer Healthcare Pharmaceuticals, Wayne, NJ, USA) bolus injection was performed by hand push at Image 15. After a data-driven process for model selection and parametric estimation (6,12,13), the slice with the largest tumor cross-section, usually the center slice, was selected for further analysis so that it might be assumed that the radial movement of CA was taking place in the plane of the image.

Numerical and statistical methods

Using data from a series of LL-MRI studies performed before and after the 2GE DCE-MRI study, voxel-by-voxel maps of T_1 pre and post contrast were generated (12,14,15). After compensation for T_2^* effects, the points of the DCE-MRI data before CA administration, and the last few points of DCE-MRI data, were calibrated against the LL T_1 estimates performed pre and post study, thus creating two points, pre and post CA administration, that were used to generate and stabilize the running estimate of $\Delta R_1(t)$ ($R_1 = 1/T_1$), which in turn was used to approximate the concentration–time curve of CA in the tissue (13).

A scaled radiological arterial input function (AIF) was used as the AIF in all studies (6,9,16,17). The starting point of the AIF was aligned with the first appearance of CA in contralateral normal tissue. A global starting point was selected, usually one or two time points after the arrival of CA. For the calculation of the pharmacokinetic parameters of the SM, i.e. the extended Tofts (10,18) or extended Patlak model, or in this paper Model 3, the next 90 points (6 min) of data were fitted by minimizing the sum squared error. For Logan plot calculations, because the Logan plot depends on the asymptotic behavior of the CA in the tissue, the entire interval of indicator uptake and clearance after the starting point was considered, with the linear last portion of the curve used to estimate V_D.

Model selection

Model selection in this experimental paradigm (DCE-MRI in a rat model of cerebral tumor) has been previously presented (6,12,13) and used to select regions of interest (ROIs) in recently published studies (11,16,19). A full description of the model selection paradigm is presented in the supplementary material.

In the SM, there are at most three parameters to be estimated: the plasma volume (v_p), the forward volumetric transfer constant (K^{trans}) and the reverse transfer constant (k_{ep}). The often-reported interstitial volume fraction v_e is computed as K^{trans}/k_{ep}, although, because information in the data that pertains to the leakage of CA to the interstitium has to do with the first and second derivatives of concentration–time data, it is the rate constant k_{ep} that is directly estimated. Consider the hierarchy of models that might prevail in the analysis of DCE-MRI data in the brain. For any one voxel, there are four possible descriptions, as follows. (0) The voxel contains little or no perfused tissue. Consequently, there is no detectable change in ΔR_1 after CA administration and no parameters are different from 0. (1) The vasculature in the voxel does not detectably leak CA across the period of observation: $v_p \neq 0$, $K^{trans} = k_{ep} = 0$. This is the case in most normal brain. (2) The vasculature in the voxel detectably leaks CA, but there is little evidence of reflux from the tissue to the vasculature: $v_p \neq 0$, $K^{trans} \neq 0$, $k_{ep} = 0$. (3) The vasculature detectably leaks CA, and there is evidence of reflux from the tissue to the vasculature. This is the full model described by the SM, $v_p \neq 0$, $K^{trans} \neq 0$, $k_{ep} \neq 0$. These models are numbered 0 through 3 to reflect the number of parameters estimated. The models are nested, both physiologically and mathematically, so they can be compared via an F-statistic (6,13), with a higher-order model selected only if it is a significantly better explanation of the data than a lower-order model.

In each voxel, one set (0–3 in number) of parameters is reported, with the choice of model driven by a model comparison performed via a non-central F-test (20). In the brain, the maps produced are a map of model selection, a nearly complete

map of plasma volume, a partial map of K^{trans} and a smaller map of v_e. See Figure 1 for an example of such maps. The element of this process that was most important to this paper was the delineation via model selection of the edge of the tumor.

Patlak and Logan plots

Patlak and Logan graphical approaches are central to inferences about model behavior. The key test employed in each graphical approach addresses the question of what portion of the data can be linearized, when plotted as a Patlak (21), extended Patlak (22) – an analysis that uses the SM – or Logan (8) plot. The portions of data where linearity prevails indicates those times in the experiments where certain critical assumptions hold.

In a region where a Patlak Model 2 plot is linear, indicator enters a last (sink) compartment and is trapped therein; only v_p and K^{trans} can be estimated. In a region where a Patlak Model 3 plot is linear, an estimate of the full set of Model 3 parameters (including v_e) is available. In a region where a Logan plot is asymptotically linear, the source and sink compartments reach an approximate equilibrium in concentration. Note that, while plasma concentration is considered the forcing function of the differential equation of the model (e.g. Equation [1] in Reference 8), if another forcing function is available the relationship still holds. For instance, if the forcing function is the concentration of indicator in an adjacent space, and that space is the source of indicator, the relationships outlined above still hold, and the portions of data where the critical assumptions hold will still plot as linear functions.

Statistical methods for the analysis of the population sample

"Signal-to-noise" (S/N) in the first echo of the 2GE DCE-MRI data prior to CA administration was assessed by measuring the average image intensity of the whole brain in the middle slice of the pack, divided by the image intensity in the portions of the image where no tissue resided. In order to allow a better sense of conditions in a tumor of about 5 mm diameter, $S/N \pm SD$ for the tumor itself was also estimated; however, because the receiver employed a surface coil, the gradient in image intensity contributed to the variance of the measure of signal. Note also that this is not the true S/N in the complex time-domain data, but it is a convenient metric that is unimodal in the true S/N.

In the 18 studies, each with two measurements made 24 h apart, the parameters of interest were V_D outside the tumor rim, and tumor exudate flux through the rim. Preliminary analyses examined differences in volume with t-tests, and correlations between volume and flow with Pearson product–moment correlation coefficients. In order to account for the effect of correlated measures due to repeated studies, the final reporting analysis utilized a generalized linear model (GLM) approach, as implemented in the library *nlme* (23) of the R statistical package (24). In comparing models produced by GLM, the Akaike information criterion (AIC) was used as a measure of goodness of fit; differences in the AIC were used to predict the probability that a model was descriptive of variation in the dependent variable.

RESULTS

S/N in the DCE-MRI experiments was about 30:1. S/N in the tumor itself was about 35 ± 4.

See Figure 1, where the results of pixel-by-pixel estimates of DCE-MRI model parameters in the brain of an athymic nude rat implanted with an U251 tumor are mapped. This animal study is chosen as typical of the 18 studies summarized in this results section, and will be used throughout to illustrate the methods employed in the analysis of the full set of studies. A second study is shown in the supplementary material. Shown left to right are estimates of v_p, K^{trans}, v_e, and model selection, where Model 1 estimates only v_p, Model 2 estimates K^{trans} and v_p, and Model 3 estimates v_e, K^{trans}, and v_p. For reasons that will be explained below, the largest slice in the tumors in our animal model nearly always showed regions with near-zero or negative estimates of v_p in the Model 2 regions. For instance, in Figure 1, the map of v_p shows a nearly complete ring of negative estimates in the Model 2 region outside the tumor. Since they imply a failure of conservation of mass, these estimates are clearly artifacts and point to a model failure, but an insight into the source of these artifacts suggests a method for estimating the distribution volume of CA in the mostly normal tissue outside rim of the tumor.

First, it should be demonstrated that the CA escapes the boundaries of the tumor. An examination of the typical histology of the U251 cerebral tumor (the hematoxylin and eosin (H&E) stained section of Fig. 2 of Reference 6, of Fig. 7S of the supplementary material, and of Fig. 2 herein) shows that, on the scale of the DCE-MRI image sets, where the pixel sizes are about 250 μm, the edge of the tumor is confined to a single pixel. The post-contrast T_1-weighted images in Reference 6, in Figure 2 herein, and in Figure 7S of the supplementary material, which were acquired about 15 min after CA injection, show a bright rim of contrast around the central lesion; the DCE-MRI data in Reference 6 show that CA leaks from the tumor across the time of the experiment, and, since the area of contrast enlarges radially over time, is transported (by advection and/or diffusion) into the surrounding normal tissue, entering a region of mostly, or entirely, normal parenchyma where the blood–brain barrier restricts its reabsorption to the vasculature.
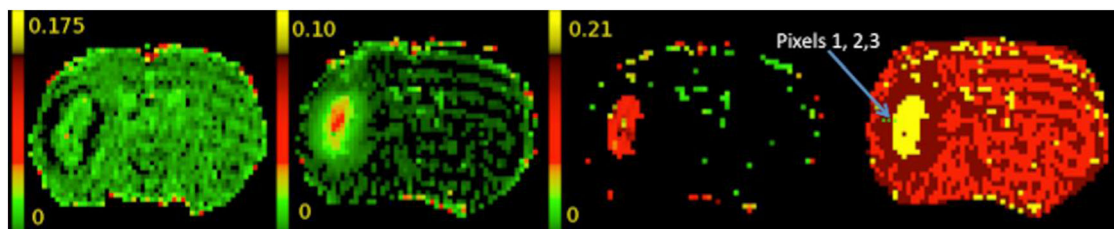

Figure 1. Parametric maps: left to right, v_p, K^{trans}, v_e and model selection. For the model selection map, yellow is Model 3 acceptance, dark red is Model 2 acceptance and red is Model 1 acceptance. In order to better display the range of values, the map of v_p was windowed to set negative values to 0. Pixels 1–3 are marked with green dots and numbered from right to left, with Pixel 1 placed in the margin of the Model 3 region, and Pixels 2 and 3 in the Mod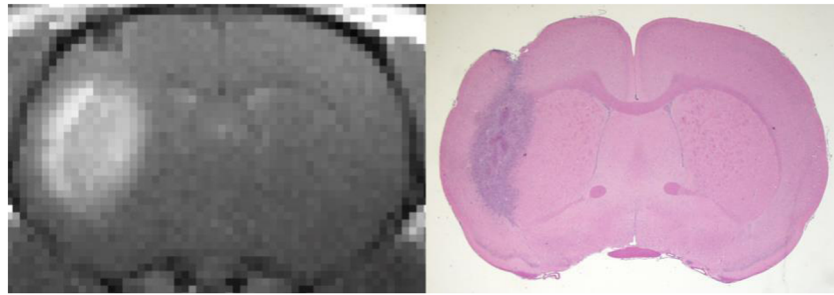el 2 region in a line proceeding from Pixel 1. Banding in the parametric maps and model selection is due to Gibbs ringing in the original 2GE data set.

Figure 2. Left: post-contrast T_1-weighted image in the animal of Figure 1. Right: H&E staining of a centrally located tissue slice. The MRI image was acquired about 15 min after the injection of CA. The central tumor mass is fairly well matched by the central but somewhat darker region of enhanced contrast, demonstrating the likely convection of the CA from the central lesion.

Notice the three pixels in Figure 1 that are marked by an arrow and three small green dots placed on the map of model selection. Figure 3 shows the change in ΔR_1 with time in the three linearly adjacent voxels, starting in the Model 3 region and proceeding outward in the Model 2 region. Two types of plot appear, with normally plotted data and curve fits in the left-hand panel, and Patlak-plotted data in the right-hand panel. In both panels, the three traces of concentration–time data correspond, top to bottom, to right to left points in Figure 1. The top trace is ΔR_1 data from Pixel 1, the Model 3 voxel; the middle trace is data from Pixel 2, the first Model 2 voxel outside the inner Model 3 region, and the bottom trace is data from Pixel 3, the next voxel out.

Presumably, the tumor is the major source of CA seen in normal tissue in Figure 2. Consider the top left ROI shown in Figure 4, defining the outer limit of the Model 3 region, outside of which is a region of predominantly Model 2 behavior with near-zero or negative estimates of v_p. Figure 5, left, displays the Patlak and extended Patlak plots of concentration–time data in this inner rim ROI, demonstrating that Model 3 provides a better explanation of the behavior of the data than Model 2 because the Model 3 plot is linear while the Model 2 plot is concave. The F-statistic, with a value of 725, yielding a vanishingly small probability that the errors of the Model 2 fit and the Model 3 fit were drawn from the same distribution, confirms this judgment. SM estimates of v_p, v_e, and K^{trans} in this inner-rim ROI are 1.1%, 10.8%, and 3.0×10^{-2} min^{-1}, respectively. The Logan plot estimate of V_D is

11.4%. These estimates reflect the typical physiology of this model of cerebral tumor, with fairly high vascular permeability, and a decreased distribution volume fraction relative to the typical 20% of normal brain tissue (25,26).

If a three-pixel-wide ROI (Fig. 4, top right) is formed outside the inner ring defined by the edge of the Model 3 region, the (Model 2) Patlak plot of Figure 6 is obtained. This plot has an evident linearity, a positive slope, a negative intercept, and a convex curve connecting the linear part of the curve to the start of the data. An examination of the methods of plotting the Patlak and extended Patlak plots shows that a convexity in the Patlak plot can only be obtained if k_{ep} is negative, a clearly non-physical situation that violates the conservation of mass and/or the assumption of temporal stability. Nevertheless, the linear portion of the Patlak plot indicates that CA is entering the region, and is not being reabsorbed by the source. It also appears that the normalized standard radiological AIF to the outer region becomes approximately correct as the experiment proceeds, but that the input to this compartment lags the input of the adjacent compartment. These observations suggest that CA enters the ROI from the adjacent inner surface, and does not re-enter the source compartment in an appreciable amount during the course of the experiment. Note that, without a model selection paradigm with its two-parameter fit resulting in a negative v_p, in a three-parameter SM analysis v_p and K^{trans} would be positive and k_{ep} negative, again signaling a model failure of standard pharmacokinetic modeling.
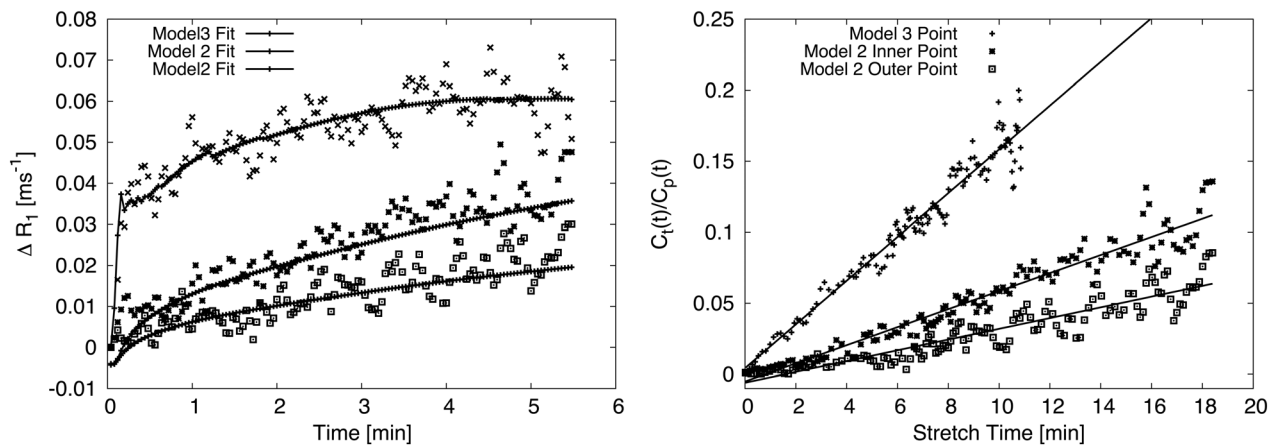

Figure 3. Left: data and curve fits from the three marked pixels of Figure 1. These three traces, top to bottom, correspond to right to left in Figure 1 – the top trace is ΔR_1 data from Pixel 1, the Model 3 voxel, the middle trace is data from Pixel 2, the first Model 2 voxel outside the inner Model 3 region, and the bottom trace is data from Pixel 3, the next voxel out. Right: linearized fits to the data showing the (Model 3) extended Patlak fit (top) and the two (Model 2) Patlak fits of the data shown on the left.
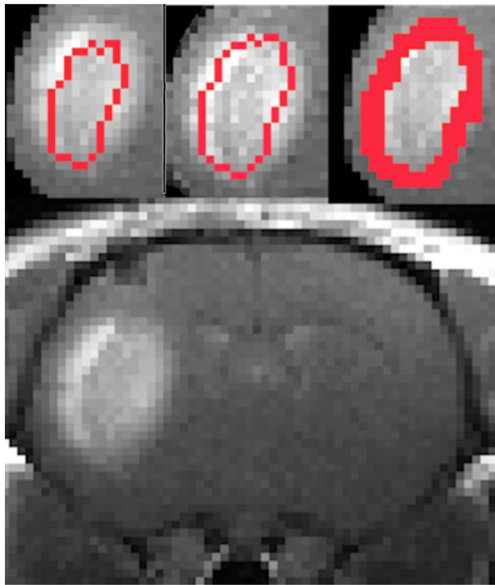
NMR IN BIOMEDICINE

Figure 4. Three ROIs in the animal under study. Left: an ROI defined as mainly Model 3, and inside the regions of negative estimate of v_p in Figure 1. Middle: an ROI of single-pixel width, adjacent to and outside of the ROI on the left, defined mainly by lying inside the regions of negative estimate of v_p. Right: the ROI of the middle panel, widened to include all of the regions of negative v_p outside the inner rim defined by the right panel. The intent of these ROIs was to define a source region (left panel), an equilibrating region (middle panel), and a sink (right panel).

Consider a thin outer ROI drawn immediately adjacent to, and outside, the ROI of the edge of the Model 3 region. This ROI, a single pixel wide, is shown as the middle panel of Figure 4. Assume that the outer ring does not contain significantly leaky vasculature, and that the inner ring supplies the thin outer ring with the majority of its CA. The Logan plot of the CA concentration in the inner ring (Fig. 5, right) shows that a transvascular equilibrium occurs where the Logan plot becomes linear, after 100 s, the 25th point post CA administration. That is to say, the CA concentrations in plasma and interstitial fluid are approximately equal after the 25th point. Thus, it is plausible that, rather than using the AIF as an input to the outer ring, the CA concentration
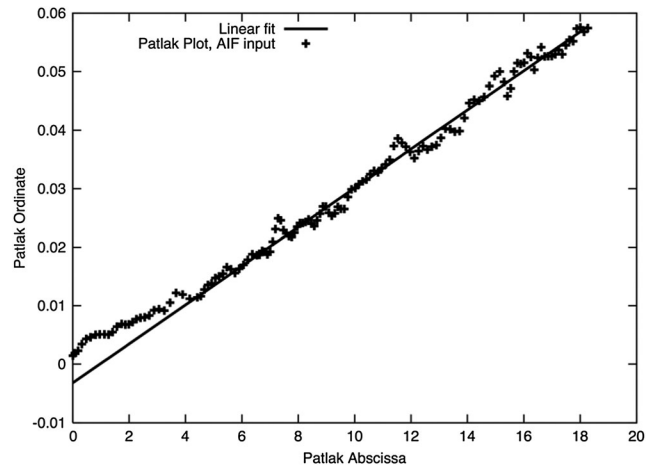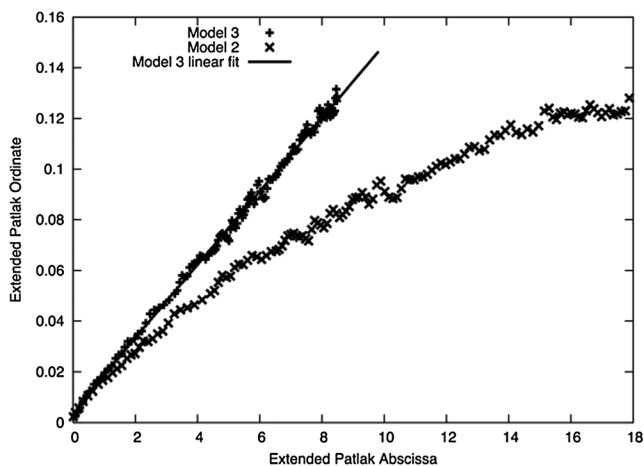

Figure 6. A Patlak plot (Model 2) of the concentration–time data in the enlarged outer rim of the tumor. The input function employed was that of the group-averaged estimate of the AIF, normalized to the plasma volume of the contralateral caudate putamen, as in Figure 5. Note the linearity of the latter part of the curve, and the convex curvature of the early part of the curve, signaling a model failure.

in the inner ring can be used as an input function, with the assumption that all the CA in the outer rim is obtained from the inner rim. It is assumed that the vascular volume of the normal contralateral caudate putamen is 1%. Since extravascular and intravascular CA concentrations have equilibrated, the extravascular concentration, i.e. the concentration of the interstitial fluid, is that of the blood. The trace of concentration in the inner ring is then normalized to be 100 times that of the trace of concentration in the (presumably non-leaky) contralateral caudate putamen. This is equivalent to requiring that the extravascular concentration of CA in the inner rim equilibrates with the intravascular concentration by the 25th point post CA injection, and that the vascular concentrations of CA do not substantially influence the behavior of the concentration–time studies under consideration. The biases introduced by vascular concentrations are examined in the appendix.

The Logan plot of Figure 7 shows the result of these procedures. The plot becomes linear after the 97th point post contrast;
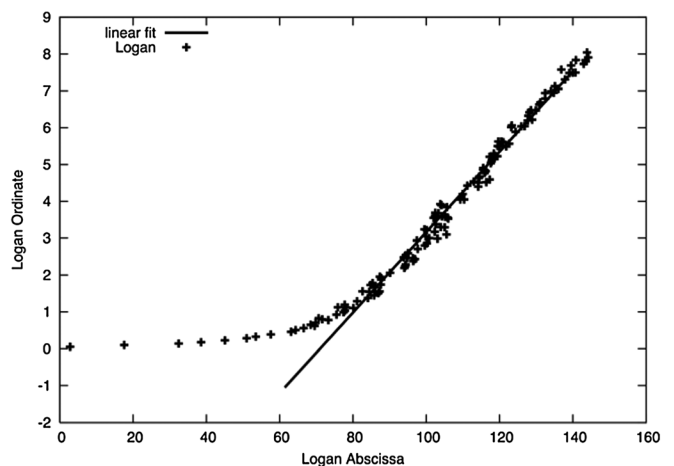

Figure 5. Left: Patlak (concave curve) and extended Patlak (linear curve) plots of response in the inner rim ROI (top left, Fig. 4). Right: Logan plot of the same data. Both plots of the data employed the group-averaged estimate of the AIF, normalized to the plasma volume of the contralateral caudate putamen.
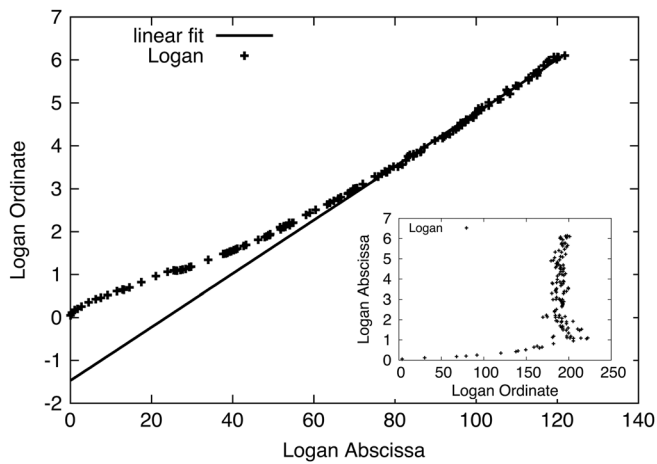
Figure 7. A Logan plot of the concentration–time data in the thin outer rim of the tumor (central ROI, Fig. 4). The input function employed was that of the normalized indicator concentration in the inner ROI. The equilibration point on the Logan ordinate of about 80 min is evident, yielding an estimate of distribution volume of about 6.4%. The same concentration–time data, plotted as a Logan plot but using the estimated plasma concentration as an input function (Figs. 5, 6), are plotted in the inset to demonstrate that the plasma concentration is not a viable input function for the concentration–time data of the thin outer rim, since the asymptotic behavior of the plot demonstrates a near-infinite slope, and thus cannot estimate distribution volume in the tissue.
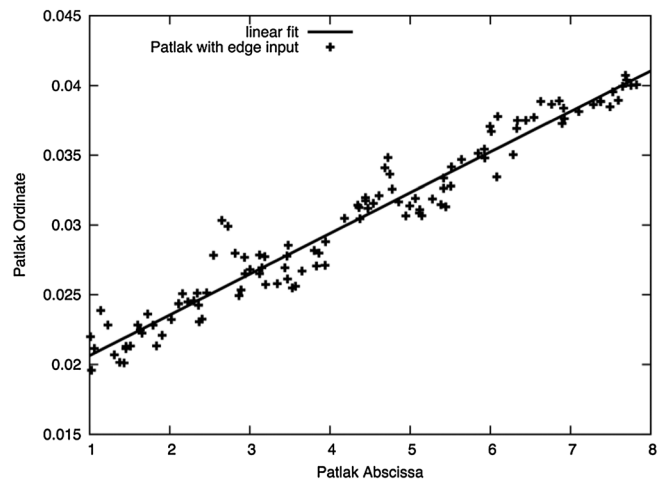

Figure 8. A Patlak plot (Model 2) of the concentration–time data in the enlarged outer rim of the tumor (top right ROI in Fig. 4), using as an input function the data of the innermost adjacent ring. The linearity of this portion of the curve is evident, thus supporting the assumptions of the model. The slope of the line yields an estimate of interstitial flow of tumor exudate.

fitting the last 35 points yields a slope of 0.0643, or an estimate of V_D of 6.4%. Contrariwise, the Logan plot of these data, but using the estimate of CA plasma concentration *versus* time that resulted in the Logan plot of Figure 5, is shown in the inset of Figure 7. This graph yields a nonsensical result because the asymptotic behavior of the plot demonstrates a near-infinite slope, and thus cannot estimate distribution volume in the tissue. This is suggestive of the inner rim being the source of CA for the outer rim.

Continuing with the practice of using the rim of the tumor as a source of CA in the adjacent outer voxels, consider the wide ROI shown in the top right-hand image of Figure 4. This ROI is 2–3 pixels wide and contains essentially all of the region outside of the tumor into which the CA leaks. Thus, it satisfies the requirements of the Patlak (Model 2) model, in that it is a final compartment from which no return to the source compartment takes place. Figure 8 shows the resulting Patlak plot, which equilibrates very quickly, and appears to be linear for almost the entirety of the experiment. The slope of the plot, 2.9×10^{-3} [ml/(ml min)] in this case, should give an estimate of the rate of transfer of the CA between the inner rim and the outer sink. When normalized to the volume of the wide ROI and the area of the interface between the inner and outer ring ROIs (see the appendix, Case 2), it yields an estimate of CA flux between the two compartments.

The compartment size (of the wide outer ROI) into which the CA flows is 134 voxels, and there are 34 voxels on the rim of the tumor. Pixel edge sizes are 32/128 mm = ¼ mm; slice thickness is 2 mm. The average flux per voxel is thus about 4.5×10^{-2} μl/(μm^2 s). Taking the estimates of interstitial volume fraction to be 6.43×10^{-2} for the outer ring and 1.14×10^{-1} for the inner ring, this rate of flux yields an estimate of fluid velocity in the interstitial space in the outer ring of 0.70 μm/s and in the inner ring of 0.37 μm/s. These velocities are in the range of other estimates of tumor velocity, i.e. less than 1 μm/s. See, for instance, Table 1 of Munson and Shieh (27) and also the work of Pishko *et al.* (28).

Table 1 summarizes the results of 34 studies in 18 animals. Sixteen of these studies were repeated studies; in Table 1 the first and second of the studies are labeled "pre" and "post," respectively. In the three parameters measured, there appeared to be no systematic differences between estimates in the two studies: that is to say that the two studies did not differ significantly in their sample means between Study 1 and Study 2 in the estimates of any parameter, nor did the paired differences show a trend by a paired *t*-test. The smallest *p*-value for any of the paired *t*-test comparisons was about 0.3 for the paired estimates of exudate flux; the smallest *p*-value for any of the tests on the sample means of Study 1 and Study 2 was about 0.17, again for flux.

The sample mean of V_D in the inner ring ROI (tumor) was about 15%; in the (presumably normal) outer ring it was about 10%. These estimates, particularly that of the outer ring, are smaller than the measured distribution volume of normal brain, which is about 20% across a wide variety of mammalian species (25,26). There were distinct differences between the estimated V_D of the inner ring region and that of the immediately adjacent outer ring. In 33 of 34 studies, the distribution volume in the outer ring ROI was smaller than its immediately adjacent inner ring ROI, and the one case where the difference was reversed was that of the second-smallest tumor cross-sectional area in the sample. In an initial analysis of parameters, the estimate of distribution volume in the inner ROI was significantly larger than that of the immediately adjacent outer ring in both Study 1 ($p < 4 \times 10^{-4}$) and Study 2 ($p < 1 \times 10^{-4}$). When calculating the difference between the inner and outer ring distribution volumes, there was no significant difference ($p = 0.63$) between Study 1 and Study 2. A GLM analysis confirmed these findings: the outer ring ROI estimate of V_D was highly predictive of the inner ring's estimate of V_D ($p < 1 \times 10^{-4}$). A regression slope of 0.528 demonstrated that the outer ring V_D was usually about half the inner ring V_D. The intercept of this relationship was non-zero (intercept = 0.021, $p \sim 0.043$), raising the possibility that some positive residual difference might be expected between the tissue of the inner (mainly tumor) and outer (mainly normal) ROIs. These analyses present a picture of a relatively porous inner ring

Table 1. Test-Retest Values of Distribution Volumes and Exudate Flux

	Dist. volume, inner edge			Dist. volume, outer edge			Inner − outer		Flux [μl/(μm^2 s)]		
	Pre	Post	Δ	Pre	Post	Δ	Pre	Post	Pre	Post	Δ
JS80		0.0691			0.0404			−0.0287		0.0151	
JS81	0.0653	0.0731	−0.0077	0.0484	0.0618	−0.0134	−0.0169	−0.0113	0.0249	0.0344	−0.0095
JS82	0.2003	0.1842	0.0160	0.1093	0.1122	−0.0029	−0.0910	−0.0720	0.0575	0.0614	−0.0039
JS83	0.1390	0.1842	−0.0452	0.0973	0.1430	−0.0456	−0.0417	−0.0413	0.0562	0.0726	−0.0164
JS87	0.1679	0.1385	0.0294	0.1552	0.1067	0.0485	−0.0127	−0.0318	0.1097	0.0641	0.0457
JS91	0.1443	0.1460	−0.0017	0.1017	0.1062	−0.0045	−0.0425	−0.0397	0.0606	0.0588	0.0018
JS93	0.1827	0.1512	0.0315	0.0842	0.0976	−0.0134	−0.0985	−0.0536	0.0509	0.0529	−0.0020
JS101	0.0767	0.0921	−0.0154	0.0498	0.0722	−0.0224	−0.0269	−0.0199	0.0264	0.0349	−0.0085
JS132	0.1065	0.1140	−0.0075	0.0762	0.0643	0.0119	−0.0304	−0.0497	0.0487	0.0452	0.0035
JS134		0.1677			0.0960			−0.0718		0.0539	
JS135	0.1335	0.1210	0.0125	0.1163	0.0669	0.0494	−0.0173	−0.0541	0.0957	0.0454	0.0504
JS162	0.1950	0.1379	0.0571	0.1833	0.1121	0.0712	−0.0118	−0.0259	0.1322	0.0817	0.0505
JS163	0.0381	0.0716	−0.0334	0.0448	0.0438	0.0010	0.0067	−0.0277	0.0350	0.0174	0.0176
JS180	0.2178	0.1956	0.0222	0.1560	0.1436	0.0124	−0.0618	−0.0520	0.1058	0.1070	−0.0012
JS181	0.1393	0.1261	0.0132	0.0835	0.0913	−0.0078	−0.0558	−0.0348	0.0479	0.0618	−0.0139
JS195	0.1163	0.1751	−0.0587	0.0789	0.1040	−0.0251	−0.0374	−0.0710	0.0474	0.0777	−0.0303
JS205	0.3011	0.2388	0.0623	0.1307	0.1468	−0.0161	−0.1704	−0.0920	0.1002	0.0835	0.0167
JS207	0.2144	0.1597	0.0547	0.1309	0.1061	0.0248	−0.0835	−0.0536	0.0891	0.0658	0.0233
Mean	0.1524	0.1414	0.0081	0.1029	0.0953	0.0042	−0.0495	−0.0472	0.0680	0.0599	0.0077
SEM	0.0166	0.0110	0.0089	0.0102	0.0075	0.0077	0.0110	0.0050	0.0327	0.0215	0.0244

of tissue that was mainly tumor, and a compressed outer ring of mainly normal tissue, in which it might be expected that the normal tissue would actually have a greater distribution volume than the tumor, absent the compressive forces placed on the outer ring by the tumor and the gradient of interstitial fluid pressure that typically exists in the rim of embedded tumors (29).

When the estimated flux from the inner ring ROI to the outer expanded ROI was considered in relation to the estimated V_D of the thin outer ring, a very significant relationship was demonstrated (see Figure 9). An R^2 of 0.9 ($N = 34$) calculated by a simple

Figure 9. Exudate flux from the inner rim of the tumor to the outer ring in 18 animals. The 16 repeated studies are connected with dashed lines. This very significant co-variance implies that a knowledge of V_D in the rim of the tumor will yield a remarkably precise prediction of exudate flow, regardless of other parameters such as TIFP and tumor porosity, which might otherwise be thought necessary for a prediction of the exudate flow rate.

regression implied that all but a small amount of the variation in flux was described by the compressed distribution volume of the outer ring. In a GLM analysis for repeated measures, a regression coefficient of 0.740 was demonstrated: V_D in the outer ring predicted ($p < 10^{-5}$) the exudate flux through the outer ring of compressed tissue. The intercept of the regression, −0.011, probably differed from 0 ($p = 0.049$). The distribution volume of the inner ring was also a strong predictor of flux ($p < 10^{-4}$), but a comparison of the two models via the AIC indicated that the outer ring V_D was a vastly better predictor than the inner ring V_D (ΔAIC = −45.5, $p = 1.7 \times 10^{-20}$). A multivariate GLM analysis that included V_D of the inner ring showed no advantage in the inclusion of that parameter in the model (ΔAIC = −8.9). Thus, the estimated distribution volume in the rim of the normal tissue bounded by the tumor in itself appears to be sufficient to predict the rate of tumor exudate flux through the rim of the tumor in this model.
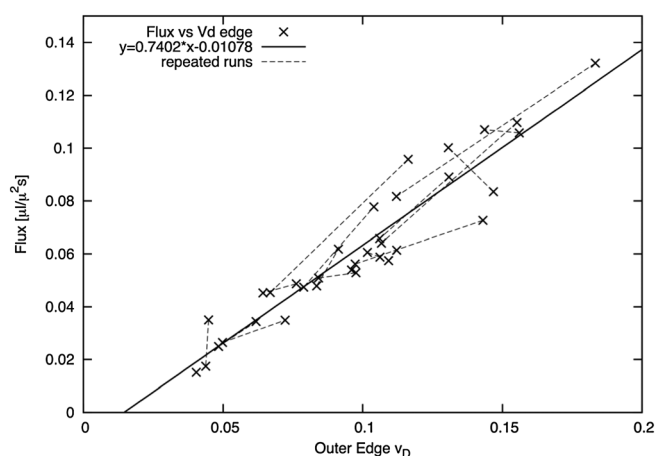
DISCUSSION

In an animal model of an embedded cerebral tumor, if its rim can be identified, a non-invasive estimate of extracellular space is available, both in the region of leaky vasculature and in the immediate boundary of that region. If its rim can be identified, an estimate of the exudate flow across the boundary of the tumor is also available. In this paper, using model selection to define the rim of the tumor, estimates of V_D of CA (porosity) in the rim of the tumor and flux through that rim resulted in the porosity strongly and independently predicting the flux.

A key reservation concerning this finding is that it is assumed that the methods in play did in fact define the rim of the tumor, and that there was little or no vascular leakage in the ROI defined as the normal tissue outside tumor edge. A better model, given sufficient S/N, would assess both transvascular leakage and

intervoxel transport. However, the information available in typical concentration–time curves is limited. It appears that two is the highest number of parameters that the data demand. The suggestion that convection and vascular leakage be modeled simultaneously appears to demand at least four variables – v_p, K^{trans}, k_{ep}, and a directed inter-voxel flow. Even in the tumor itself, typical values of R^2 are 0.98 and above (6,13), so, given the S/N of a typical experiment, a stable estimate of four or more model parameters appears unlikely (6). It is possible that poroelastic modeling, given a starting-point estimate of distribution volumes (porosities), mechanical properties of tissue, and the time-dependent spatial concentrations of CA, might be employed to make a best-guess estimate of TIFP, intervoxel convection, and microvascular permeability (28,30–32). This appears to be a natural extension of the work presented herein, but one notes that the S/N is limited in MRI studies of contrast transport, posing significant problems in extended modeling that uses dynamic MRI data for verification.

Although it has been of secondary interest in DCE-MRI, voxel-to-voxel transport of CA has been noted in cerebral tumors, sometimes as a source of artifact (6,33), but also as a potential means of assessing tumor interstitial pressure (1–3) and/or evaluating tumor characteristics that affect the delivery of chemotherapy (30,34–36) and bias parametric estimates in DCE-MRI (30,34). One experimental measure that affects all these considerations is the extracellular volume fraction, particularly because it can be expected that this quantity, equivalent to the porosity (φ) of the tissue when the tissue is studied as a poroelastic medium (31,37), is related to the fluid conductivity of the medium (5). In the absence of *in vivo* experimental evidence, fluid conductivity is sometimes modeled as a constant across tissues (see, e.g., Reference 30), and also the supplementary material of Reference 38), which may lead to biased results.

In vivo experimental estimates of porosity in tumors and normal tissues are relatively scarce. In humans, a positron emission tomography (PET) study using [76]Br-bromide studied nine patients with cerebral tumors of varying grades, usually after bulk resection, and adjuvant therapy (39). ROIs were chosen to incorporate the highest concentration of radiotracer, so estimates of extracellular volume in the tumor, which ranged from 16% to 62%, might be expected to be biased high. Estimates of extracellular volume in normal brain, about 20%, were in agreement with classical measures in the brains of a wide variety of animal species (25,26). While this *in vivo* human study is interesting, the choice to inspect regions of highest [76]Br uptake, coupled to the limited intrinsic resolution of PET, and the treatments, particularly tumor resection, that the patients in this group had undergone, shed little light on tissue porosity and/or exudate flux at the rim of the tumor. Note also that a DCE-MRI study in patients with glioma (40) assessed interstitial volume in tumors as having two types of filling – the faster filling compartments had much lower values than the PET study, while the slower filling compartments tended to agree with the PET study, raising the likelihood that slowly filling necrotic regions were better sensed in the PET study.

An investigation in a rat model of cerebral glioma ($N = 4$) employing a 9L gliosarcoma cell line performed DCE-MRI studies at 4.7 T with similar timing and CA to the work herein, but with a different analysis (BOLERO (41)) that included the effects of water exchange. This study yielded much larger estimates of v_e than those that appear herein, with porosity estimates of about 0.5. This large interstitial volume fraction seems implausible when viewing histology of the closely packed cells of a 9L

cerebral tumor. A later paper (42) using a water exchange model (BALDERO) (43) with all three eigenvalues in play and a normalized AIF estimated v_e in a U87 cerebral tumor model to be about 15%, in fair agreement with this and other studies. We note that the estimates of K^{trans} herein and in other publications that use the SM to study both human and animal models of cerebral tumor (6,11,13,16) are in fairly good agreement with those of computer-assisted tomography perfusion estimates (44) that use a similarly sized CA with no dependence on water exchange.

Some additional discussion is warranted by the concern that variation between the true AIFs in individual studies and the group-averaged AIF that was employed throughout the sample undermines the results of these studies. The most straightforward approach to this topic is to refer to the tables of Reference 11). That work contains a statistical analysis of the 24 h test–retest variation in the sample of animals presented in this paper. In Model 3 regions, paired differences were not significantly different from 0 for any of the model parameters, or for either of the summary statistics (mean, median). For K^{trans} and v_e (Tables 2 and 3 of Reference 11), the sample of paired differences displayed very small medians and means, less than 3% for K^{trans} and about 5% for v_e. The parameter v_p showed higher sampling differences – about 15% in the mean, which might be expected of a parameter that, unlike K^{trans} and v_e, is sensitive to the high-frequency components of the AIF. Test–retest areas of Model 3 did not differ. Thus, the sample of animals used in this present paper does not present a picture of high variability in the parametric estimates of the Model 3 region. A summary of Model 2 parameters and areas also did not show large sampling mean differences. This implies that the underlying processes involved in the DCE-MRI studies were stable, and should alleviate concern about the influence of hand injection of CA.

There are sound physical reasons to explain the experiment's insensitivity to the details of the shape of the input function. The transfer of CA to the interstitium constitutes a low-pass filter – the components of the input function that are passed to the interstitium are the ones with long time constants. In the Model 3 regions (i.e. in the tumors) of both humans (13) and animals (6), R^2 values of 0.98 and higher are typical for a 6 min DCE-MRI analysis, so the low-pass filter explains almost the entirety of the signal behavior in the experiment. In both humans (13) and animals (6), typical rate constants for transfer of CA to and from tissue (K^{trans} and k_{ep}) in the tumor are less than 0.1 min^{-1}, meaning that the components of the input function that are important in Model 3 regions are those with time constants of about 10 min or longer. The most important element of the input function is the DC component; the short-term details of the shape of the input function do not contribute strongly to the fitting of the major component of the tissue response. In order to reliably estimate the DC component of the input function, we utilize the very useful *a priori* knowledge that CA does not leak from the vasculature in normal tissue across the 6 min time of the experiment (45), and that the plasma volume in the caudate putamen is approximately 1% (46). These matters are further explained in the supplementary material.

Figure 9, displaying 32 samples in 16 animals, appears to describe a major effect in the physiology of an embedded cerebral tumor; about 90% of the variation is explained by one relationship. That a decreased distribution volume in the rim of a tumor so strongly predicts tumor exudate flux generates a puzzle in modeling. If one infers that tumor rim compression governs exudate flux to the practical exclusion of other effects, what then

is the role of T, or of the solid stresses generated by tumor growth? Measures of TIFP in this model (data not shown) are generally in the range of 5–15 mm Hg, and cellularity is also known to vary – Table 1 shows a factor of 4 in V_D in the inner rim ROI. Since cellularity and V_D co-vary (11), it is likely that tumor rim cellularity varied substantially, and, along with this variation, tumor rim compression due to hyper-cellularity varied from animal to animal. Further, a number of constraints having to do with the nature of the input function in the dynamic models were placed on the analysis of data, probably introducing a variation in those animals whose input function deviated from the assumptions necessary for the analysis. Despite these other likely variations, it appears that one parameter, the distribution volume in the rim beyond the tumor, was predictive of the great majority of the variation in the rate of exudate flux from the tumor.

One explanation for these data is that perfusion, i.e. the *delivery* of blood to the tumor, was regulated by the compression of the tumor rim, and that the total exudate flow was limited by total perfusion. It has been demonstrated that TIFP is regulated by perfusion pressure (47). It can be reasoned that TIFP, exudate flow, and compression of the tumor rim all co-vary in a fashion that depends on the relative mechanical properties of the tumor and its surroundings. This paper is not the place to carry out a poroelastic analysis of the range of possibilities, but we note that, in many tumors, the rigidity of the extracellular matrix, and of the tumor itself, is greater than that of the normal tissue in which the tumor is embedded, and that modeling of solid stresses in tumors predict that "elevated radial and circumferential stress levels extend beyond the tumor by at least one tumor radius" (31). If this is the case with the U251 tumors studied in this work, then a picture is presented of a relatively incompressible, albeit tightly packed, tumor surrounded by a layer of relatively compliant tissue whose mechanical properties essentially regulate flow into, flow out of, and interstitial fluid pressure within the tumor.

Note that U251 tumors of the size that were studied, 5–8 mm diameter, typically have necrotic cores. Thus, these embedded tumors may not have had the central support that has been modeled in solid tumors (31,38). It may be that, without that central support, the solid stress associated with proliferating cells assumes less importance than the solid stress associated with a pressure gradient that projects into the normal surround of an embedded tumor.

A number of fairly strong constraints have been placed on the analysis of data in this work. Many of these have to do with the nature of the input function to the system being studied. In estimating K^{trans}, k_{ep}, v_p, and V_D in the Model 3 region, it was assumed that a group-averaged AIF would serve adequately for individual input functions. It was also assumed that the integrated tissue response in the (presumably) non-leaky caudate putamen would serve to scale the group-averaged input function (by a factor of 100). In the Model 2 region, it was assumed that no vascular leakage occurred, that the sole source of contrast was the adjacent inner region, and that the contrast concentration of the inner rim could also be scaled to the contrast of the caudate putamen. It was assumed that, for the time of the experiment, all of the tumor exudate remained within the bounds of an extended ROI drawn around the inner rim, and also that, at some time after the equilibration of the inner rim's extra- and intravascular concentrations, the amount of indicator flowing into, and out of, the thin outer rim equilibrated. Many of these assumptions and constraints are reasonable, based on the linearities in the data analysis that tend to confirm them, and on the generation of an orderly set of inferences that, in their internal consistency, tend to support the assumptions. However, some caution is necessary: these observations should be replicated in other tumors and tissues, and, where practical, be compared with other measures of exudate flow.

We note the benefit of using the model selection paradigms that were employed in this effort. The boundary of the Model 3 region apparently serves as a discriminant between tumor and normal parenchyma, and provides a clear choice for the location of a driving function of tumor exudate flow. Model selection in the GLM analyses also helped to provide a clear picture of the relative strengths of the associations between measured parameters, and allowed a clear path to the inferred relationships between flow and V_D. A model selection procedure generated an observation, the negative values of v_p in the Model 2 rim of the tumor, that led to the hypothesis that CA was streaming from the leaky inner rim to the non-leaky outer rim, and thence to the ability to estimate V_D in the boundary region of the tumor.

These results prompt a cautionary comment about the costs of employing *a priori* knowledge in model fitting. It does seem to make sense in the analysis of DCE-MRI data to at least bound the search space to physically possible values, and non-negative constraints are almost universally employed in DCE-MRI. Note, however, that estimates that lie outside those bounds signal that a fundamental mismatch between model and measurement has occurred; the work herein would probably not have been generated if there had been a non-negative constraint on the parameter estimates. That said, it would be quite possible, if another reliable way to define the edge of the tumor could be described, to proceed to estimate tissue compression and flux in the boundary of the tumor. It appears that the information contained in that analysis constitutes a description of tumor physiology, and probably of changes in tumor physiology under treatment.

Acknowledgements

References

1. Hassid Y, Furman-Haran E, Margalit R, Eilam R, Degani H. Noninvasive magnetic resonance imaging of transport and interstitial fluid pressure in ectopic human lung tumors. Cancer Res. 2006; 66(8): 4159–4166.
2. Hompland T, Ellingsen C, Rofstad EK. Preclinical evaluation of Gd-DTPA and gadomelitol as contrast agents in DCE-MRI of cervical carcinoma interstitial fluid pressure. BMC Cancer 2012; 12(1): 544.
3. Hompland T, Ellingsen C, Ovrebo KM, Rofstad EK. Interstitial fluid pressure and associated lymph node metastasis revealed in tumors by dynamic contrast-enhanced MRI. Cancer Res. 2012; 72(19): 4899–4908.
4. Liu LJ, Brown SL, Ewing JR, Schlesinger M. Phenomenological model of interstitial fluid pressure in a solid tumor. Phys. Rev. E 2011; 84(2): 021919-021911–021919-021919.
5. Nield DA, Bejan A. *Convection in Porous Media*, 3rd edn. Springer: New York, 2006.
6. Ewing JR, Bagher-Ebadian H. Model selection in measures of vascular parameters using dynamic contrast-enhanced MRI: experimental and clinical applications. NMR Biomed. 2013; 26(8): 1028–1041.

7. Logan J. Graphical analysis of PET data applied to reversible and irreversible tracers. Nucl. Med. Biol. 2000; 27(7): 661–670.

8. Logan J, Fowler JS, Volkow ND, Wolf AP, Dewey SL, Schlyer DJ, MacGregor RR, Hitzemann R, Bendriem B, Gatley SJ, Christman DR. Graphical analysis of reversible radioligand binding from time-activity measurements applied to [N-11C-methyl]-(−)-cocaine PET studies in human subjects. J. Cereb. Blood Flow Metab. 1990; 10(5): 740–747.

9. Aryal MP, Nagaraja TN, Keenan KA, Bagher-Ebadian H, Panda S, Brown SL, Cabral G, Fenstermacher JD, Ewing JR. Dynamic contrast enhanced MRI parameters and tumor cellularity in a rat model of cerebral glioma at 7 T. Magn. Reson. Med. 2014; 71(6): 2206–2214.

10. Tofts PS, Brix G, Buckley DL, Evelhoch JL, Henderson E, Knopp MV, Larsson HB, Lee TY, Mayr NA, Parker GJ, Port RE, Taylor J, Weisskoff RM. Estimating kinetic parameters from dynamic contrast-enhanced T_1-weighted MRI of a diffusable tracer: standardized quantities and symbols. J. Magn. Reson. Imaging 1999; 10(3): 223–232.

11. Aryal MP, Nagaraja TN, Brown SL, Lu M, Bagher-Ebadian H, Ding G, Panda S, Keenan K, Cabral G, Mikkelsen T, Ewing JR. Intratumor distribution and test–retest comparisons of physiological parameters quantified by dynamic contrast-enhanced MRI in rat U251 glioma. NMR Biomed. 2014; 27(10): 1230–1238.

12. Ewing JR, Brown SL, Lu M, Panda S, Ding G, Knight RA, Cao Y, Jiang Q, Nagaraja TN, Churchman JL, Fenstermacher JD. Model selection in magnetic resonance imaging measurements of vascular permeability: Gadomer in a 9 L model of rat cerebral tumor. J. Cereb. Blood Flow Metab. 2006; 26(3): 310–320.

13. Bagher-Ebadian H, Jain R, Nejad-Davarani SP, Mikkelsen T, Lu M, Jiang Q, Scarpace L, Arbab AS, Narang J, Soltanian-Zadeh H, Paudyal R, Ewing JR. Model selection for DCE-T1 studies in glioblastoma. Magn. Reson. Med. 2012; 68(1): 241–251.

14. Gelman N, Ewing JR, Gorell JM, Spickler EM, Solomon EG. Inter-regional variation of longitudinal relaxation rates in human brain at 3.0 T: relation to estimated iron and water contents. Magn. Reson. Med. 2001; 45(1): 71–79.

15. Ewing JR, Brown SL, Nagaraja TN, Bagher-Ebadian H, Paudyal R, Panda S, Knight RA, Ding G, Jiang Q, Lu M, Fenstermacher JD. MRI measurement of change in vascular parameters in the 9L rat cerebral tumor after dexamethasone administration. J. Magn. Reson. Imaging. 2008 27(6): 1430–1438.

16. Nagaraja TN, Aryal MP, Brown SL, Bagher-Ebadian H, Mikkelsen T, Yang JJ, Panda S, Keenan KA, Cabral G, Ewing JR. Cilengitide-induced temporal variations in transvascular transfer parameters of tumor vasculature in a rat glioma model: identifying potential MRI biomarkers of acute effects. PLoS One 2013; 8(12): e84493.

17. Nagaraja TN, Karki K, Ewing JR, Divine GW, Fenstermacher JD, Patlak CS, Knight RA. The MRI-measured arterial input function resulting from a bolus injection of Gd-DTPA in a rat model of stroke slightly underestimates that of Gd-[(14)C]DTPA and marginally overestimates the blood-to-brain influx rate constant determined by Patlak plots. Magn. Reson. Med. 2010; 63(6): 1502–1509.

18. Sourbron SP, Buckley DL. Classic models for dynamic contrast-enhanced MRI. NMR Biomed. 2013; 26(8): 1004–1027.

19. Brown SL, Nagaraja TN, Aryal MP, Panda S, Cabral G, Keenan KA, Elmghirbi R, Mikkelsen T, Hearshen D, Knight RA, Wen N, Kim JH, Ewing JR. MRI-tracked tumor vascular changes in the hours after single-fraction irradiation. Radiat. Res. 2015; 183(6): 713–721.

20. Scheffé H. *The Analysis of Variance*, Bradley RA, Hunter JS, Kendall DG, Watson GS (eds). Wiley: New York, 1959.

21. Patlak CS, Blasberg RG, Fenstermacher JD. Graphical evaluation of blood-to-brain transfer constants from multiple-time uptake data. J. Cereb. Blood Flow Metab. 1983; 3: 1–7.

22. Patlak C, Blasberg R. Graphical evaluation of blood to brain transfer constants from multiple-time uptake data. Generalizations. J. Cereb. Blood Flow Metab. 1985; 5: 584–590.

23. Pinheiro J, Bates DB, DebRoy SD, Sarkar D, R Core Team. nlme: Linear and Nonlinear Mixed Effects Models. R package. 2013.

24. R Core Team. *R. A Language and Environment for Statistical Computing*. R Foundation For Statistical Computing: Vienna, 2013.

25. Levin VA, Fenstermacher JD, Patlak CS. Sucrose and inulin space measurements of cerebral cortex in four mammalian species. Am. J. Physiol. 1970; 219(5): 1528–1533.

26. Sykova E, Nicholson C. Diffusion in brain extracellular space. Physiol. Rev. 2008; 88(4): 1277–1340.

27. Munson JM, Shieh AC. Interstitial fluid flow in cancer: implications for disease progression and treatment. Cancer Manag. Res. 2014; 6: 317–328.

28. Pishko GL, Astary GW, Mareci TH, Sarntinoranont M. Sensitivity analysis of an image-based solid tumor computational model with heterogeneous vasculature and porosity. Ann. Biomed. Eng. 2011; 39(9): 2360–2373.

29. Boucher Y, Baxter LT, Jain RK. Interstitial pressure gradients in tissue-isolated and subcutaneous tumors: implications for therapy. Cancer Res. 1990; 50(15): 4478–4484.

30. Pishko GL, Astary GW, Zhang J, Mareci TH, Sarntinoranont M. Role of convection and diffusion on DCE-MRI parameters in low leakiness KHT sarcomas. Microvasc. Res. 2012; 84(3): 306–313.

31. Sarntinoranont M, Rooney F, Ferrari M. Interstitial stress and fluid pressure within a growing tumor. Ann. Biomed. Eng. 2003; 31(3): 327–335.

32. Netti PA, Berk DA, Swartz MA, Grodzinsky AJ, Jain RK. Role of extra-cellular matrix assembly in interstitial transport in solid tumors. Cancer Res. 2000; 60(9): 2497–2503.

33. Pronin IN, McManus KA, Holodny AI, Peck KK, Kornienko VN. Quantification of dispersion of Gd-DTPA from the initial area of enhancement into the peritumoral zone of edema in brain tumors. J. Neurooncol 2009; 94(3): 399–408.

34. Magdoom KN, Pishko GL, Rice L, Pampo C, Siemann DW, Sarntinoranont M. MRI-based computational model of heterogeneous tracer transport following local infusion into a mouse hind limb tumor. PLoS One 2014; 9(3): e89594.

35. Sirianni RW, Zheng MQ, Saltzman WM, Huang Y, Carson RE. Direct, quantitative, and noninvasive imaging of the transport of active agents through intact brain with positron emission tomography. Mol. Imaging Biol. 2013; 15(5): 596–605.

36. Pathak AP, Artemov D, Ward BD, Jackson DG, Neeman M, Bhujwalla ZM. Characterizing extravascular fluid transport of macromolecules in the tumor interstitium by magnetic resonance imaging. Cancer Res. 2005; 65(4): 1425–1432.

37. Netti PA, Baxter LT, Boucher Y, Skalak R, Jain RK. Time-dependent behavior of interstitial fluid pressure in solid tumors: implications for drug delivery. Cancer Res. 1995; 55(22): 5451–5458.

38. Stylianopoulos T, Martin JD, Snuderl M, Mpekris F, Jain SR, Jain RK. Coevolution of solid stress and interstitial fluid pressure in tumors during progression: implications for vascular collapse. Cancer Res. 2013; 73(13): 3833–3841.

39. Bruehlmeier M, Roelcke U, Blauenstein P, Missimer J, Schubiger PA, Locher JT, Pellikka R, Ametamey SM. Measurement of the extracellular space in brain tumors using ^{76}Br-bromide and PET. J. Nucl. Med. 2003; 44(8): 1210–1218.

40. Ludemann L, Grieger W, Wurm R, Budzisch M, Hamm B, Zimmer C. Comparison of dynamic contrast-enhanced MRI with WHO tumor grading for gliomas. Eur. Radiol. 2001; 11(7): 1231–1241.

41. Yankeelov TE, Rooney WD, Li X, Springer CS. Variation of the relaxographic "shutter-speed" for transcytoliemmal water exchange affects the CR bolus-tracking curve shape. Magn. Reson. Med. 2003; 50(6): 1151–1169.

42. Li X, Rooney WD, Varallyay CG, Gahramanov S, Muldoon LL, Goodman JA, Tagge IJ, Selzer AH, Pike MM, Neuwelt EA, Springer CS, Jr. Dynamic-contrast-enhanced-MRI with extravasating contrast reagent: rat cerebral glioma blood volume determination. J. Magn. Reson. 2010; 206(2): 190–199.

43. Li X, Rooney WD, Springer CS, Jr. A unified magnetic resonance imaging pharmacokinetic theory: intravascular and extracellular contrast reagents. Magn. Reson. Med. 2005; 54(6): 1351–1359.

44. Jain R, Ellika SK, Scarpace L, Schultz LR, Rock JP, Gutierrez J, Patel SC, Ewing J, Mikkelsen T. Quantitative estimation of permeability surface–area product in astroglial brain tumors using perfusion CT and correlation with histopathologic grade. Am. J. Neuroradiol. 2008; 29(4): 694–700.

45. Blasberg RG, Fenstermacher JD, Patlak CS. Transport of alpha-aminoisobutyric acid across brain capillary and cellular membranes. J. Cereb. Blood Flow Metab. 1983; 3(1): 8–32.

46. Bereczki D, Wei L, Otsuka T, Hans F-J, Acuff V, Patlak C, Fenstermacher J. Hypercapnia slightly raises blood volume and sizably elevates flow velocity in brain microvessels. Am. J. Physiol. 1993; 264: H1360–H1369.

47. Boucher Y, Salehi H, Witwer B, Harsh GR, Jain RK. Interstitial fluid pressure in intracranial tumours in patients and in rodents. Br. J. Cancer 1997; 75(6): 829–836.

SUPPORTING INFORMATION

Additional supporting information can be found in the online version of this article at the publisher's website.

APPENDIX

CASE 1. THE LOGAN PLOT IN THE THIN RIM

See Figure 10, Case 1. In Case 1, fluid carries an indicator from Compartment 1 to Compartment 2. The dimensions of Compartment 2 are small compared with the velocity of the fluid so that, after a short time, the indicator begins to exit Compartment 2. When the slope of the input function to Compartment 2 begins to change slowly, approximately the same amount of indicator is leaving the compartment as is entering it. This is an equilibrium condition that can be exploited to evaluate the distribution volume of Compartment 2.

Assume that there is no leakage from the microvasculature in Compartment 2, that intravascular concentration of indicator can be ignored, and that indicator flows only from Compartment 1 to Compartment 2, and thence to a sink. In a differential time interval, the change in the quantity $Q_2(t)$ of the indicator is equal to the difference between the quantity entering, and the quantity leaving the compartment:

$$dQ_2(t) = F[C_{1e}(t) - C_{2e}(t)], \qquad [1]$$

where F is the flow from Compartment 1 to Compartment 2, and $C_{1e}(t)$ and $C_{2e}(t)$ are the concentrations of indicator in the extracellular interstitial fluid of Compartment 1 and Compartment 2, respectively.

Integrating and dividing by the volume of the second compartment,

$$\frac{Q_2(t)}{V_2} = \frac{F}{V_2}\left[\int_0^t C_{1e}(\tau)d\tau - \int_0^t C_{2e}(\tau)d\tau\right] + \frac{V_{2p}}{V_2}C_{2p}(t),$$

generates an expression in concentrations and specific flows:

$$C_2(t) = f\left[\int_0^t C_{1e}(\tau)d\tau - \int_0^t C_{2e}(\tau)d\tau\right] + v_{2p}C_{2p}(t), \qquad [2]$$

where in Compartment 2 V_2 is the volume, V_{2p} is the plasma volume, f is the specific flow [ml/(ml min)], and v_{2p} is the fractional
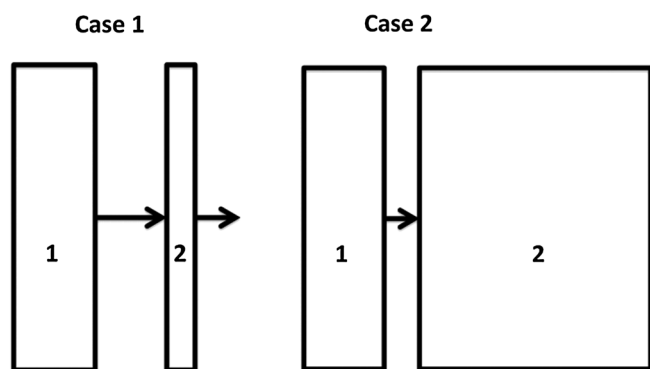
Case 1   Case 2

Figure A1. A two-compartment system. In Case 1, CA flows into, and out of, Compartment 2. After some time t_1^*, the vascular concentration of CA in Compartment 1 equilibrates with its interstitial concentration. After some time t_2^*, the inflow and outflow of CA in Compartment 2 is approximately equilibrated. The equilibration is demonstrated by the Logan plot of this data becoming linear. In Case 2, CA flows into Compartment 2, but is not cleared from the compartment. After some time t', a Patlak plot (Model 2) becomes linear.

plasma volume. By convention, lower-case letters are associated with quantities that are normalized to volumes. Initially, consider only the interstitial concentrations (i.e., assume $v_{2p} = v_{1p} = 0$, where v_{ip} is the fractional plasma volume of the ith compartment). Continuing,

$$\frac{C_2(t)}{f} = \int_0^t C_{1e}(\tau)d\tau - \int_0^t C_{2e}(\tau)d\tau, \qquad [3]$$

note that $C_2(t) = v_{2e}C_{2e}(t)$, where v_{2e} is the fractional volume of the interstitial space in Compartment 2 and $C_2(t)$ is the concentration of indicator in Compartment 2. Dividing both sides of the equation by $C_2(t)$ and transposing two terms yields an equation in the form proposed by Logan (8).

$$\frac{\int_0^t C_2(\tau)d\tau}{C_2(t)} = \frac{v_{2e}\int_0^t C_{1e}(\tau)d\tau}{C_2(t)} - \frac{v_{2e}}{f}. \qquad [4]$$

Under the assumption that the concentration of CA has equilibrated between inflow and outflow, and that $v_{1p} = v_{2p} = 0$, a Logan plot with $\frac{\int_0^t C_2(\tau)d\tau}{C_2(t)}$ on the ordinate and $\frac{\int_0^t C_{1e}(\tau)d\tau}{C_2(t)}$ on the abscissa will yield a straight line with a slope of v_{2e}.

The interstitial concentration in Compartment 1, $C_{1e}(t)$, is related to the tissue concentration, $C_1(t)$, via the relation $C_1(t) = v_{1e}C_{1e}(t)$. An estimate of v_{1e} is available through the Model 3 analysis, but there is a more reliable estimate of $C_{1e}(t)$ that can be obtained through its behavior as described by a Logan plot. In the case at hand, an examination of the Logan plot of indicator concentration in the Model 3 region (i.e. Compartment 1) at the edge of the tumor demonstrates that the exudate fluid in Compartment 1 equilibrates with the plasma concentration. That is, the Logan plot of Compartment 1 becomes linear, with a slope of V_D, at times $t > t_1^*$. Given this, the same tactic that applies to calibrating $C_p(t)$, i.e. scaling an input function to a large area of normal caudate putamen, with the assumption that v_p in the caudate putamen is 1% of tissue volume, can be applied to the section of $C_1(t)$ where $t > t_1^*$. This practice was followed throughout in estimating the interstitial space at the rim of the tumor.

It should be noted that only $C_1(t)$, $C_2(t)$, and (indirectly) $C_p(t)$ are observable. The presence of a non-zero vascular volume, filled with CA, introduces a bias into the result above.

Generally, since Compartments 1 and 2 are adjacent, we can assume that the plasma concentrations in the two compartments are approximately equal. Thus $C_{1p}(t) = C_{2p}(t) = C_p(t)$. The quantities of CA in Compartments 1 and 2, respectively, are

$$Q_1(t) = V_{1p}C_p(t) + V_{1e}C_{1e}(t)$$
$$Q_2(t) = V_{2p}C_p(t) + V_{2e}C_{2e}(t).$$

Dividing each by the volume of its compartment yield the following relationships between the measureable quantities $C_1(t)$ and $C_2(t)$ and the quantities of interest, $C_{1e}(t)$ and $C_{2e}(t)$:

$$C_{1e}(t) = \frac{C_1(t) - v_{1p}C_p(t)}{v_{1e}} \quad \text{and} \quad C_{2e}(t)$$
$$= \frac{C_2(t) - v_{2p}C_p(t)}{v_{2e}}. \qquad [5]$$

From Equations [2] and [5],

$$\frac{C_2(t)}{f} = \frac{1}{v_{1e}}\int_0^t \left[C_1(\tau) - v_{1p}C_p(\tau)\right]d\tau - \frac{1}{v_{2e}}\int_0^t \left[C_2(\tau) - v_{2p}C_p(\tau)\right]d\tau$$
$$+ \frac{v_{2p}C_p(t)}{f}.$$

Rearranging and collecting terms to generate an equation in the form of a Logan plot,

$$\frac{\int_0^t C_2(\tau)d\tau}{C_2(t)} = \frac{v_{2e}\int_0^t \frac{C_1(\tau)}{v_{1e}}d\tau}{C_2(t)} + v_{2e}\left(\frac{v_{2p}}{v_{2e}} - \frac{v_{1p}}{v_{1e}}\right)\frac{\int_0^t C_p(\tau)d\tau}{C_2(t)}$$
$$- \frac{v_{2e}}{f}\left(1 - \frac{v_{2p}C_p(t)}{C_2(t)}\right).$$

As before, the quantity $\frac{C_1(t)}{v_{1e}}$ is estimated after the equilibration of plasma and interstitial concentrations in Compartment 1, and set equal to $C_p(t)$. This yields an equation in the form of a Logan plot equation:

$$\frac{\int_0^t C_2(\tau)d\tau}{C_2(t)} = \frac{v_{2e}\int_0^t \alpha C_1(\tau)d\tau}{C_2(t)} + v_{2e}\left(\frac{v_{2p}}{v_{2e}} - \frac{v_{1p}}{v_{1e}}\right)\frac{\int_0^t C_p(\tau)d\tau}{C_2(t)}$$
$$- \frac{v_{2e}}{f}\left(1 - \frac{v_{2p}C_p(t)}{C_2(t)}\right), \qquad [6]$$

where α is the factor that scales the measured change in contrast in Region 1 to the known concentration, that of the plasma, after time $t1^*$. Thus, a Logan plot with $\frac{\int_0^t C_2(\tau)d\tau}{C_2(t)}$ on the ordinate and $\frac{\int_0^t \alpha C_1(\tau)d\tau}{C_2(t)}$ on the abscissa, with α adjusted to equal plasma concentration, when the conditions of the assumption are met (flow of contrast into and out of Compartment 2 is balanced), coupled with a slowly changing plasma concentration, will yield a straight line with a slope of $v_{2e}\left(1 + \frac{v_{2p}}{v_{2e}} - \frac{v_{1p}}{v_{1e}}\right)$. The interstitial volume fraction actions $v2e$ and $v1e$ are generally larger than their respective plasma volume fractions (typically a factor of 10 or more). Thus, assuming the worst case of $v1p = 0$, with the other compartment ratio of relative volumes around 1/10, there is an upper limit on the error introduced by the presence of CA in Compartments 1 and 2 of about 10%. Generally speaking, since $v2p \approx v1p$, the error can be expected to be much smaller than 10%.

JS132			
v_{1p}	v_{2p}	v_{1e}	v_{2e}
0.0110	0.01 (est.)	0.114	0.0642

CASE 2. THE PATLAK PLOT IN THE WIDE RIM

In Case 2, no contrast exits from Compartment 2, considerably simplifying the treatment of the model. We ignore for the time being the plasma volume of Compartment 1, V_{1p}.

$$dQ_2(t) = FC_{1e}(t)dt \qquad [7]$$

$$Q_2(t) = F\int_0^t C_{1e}(\tau)d\tau + V_{2p}C_{2p}(t). \qquad [8]$$

Normalizing to the volume of the second compartment and dividing both sides by $C_{2p}(t)$ yields the Patlak (Model 2) equation.

$$\frac{C_2(t)}{C_{2p}(t)} = f\frac{\int_0^t C_{1e}(\tau)d\tau}{C_{2p}(t)} + v_{2p}.$$

Remembering once again that $C_{1e}(t)$ is known to equilibrate with the plasma concentration, we can say that after a time t_1^* the relationship $\frac{C_2(t)}{C_{1e}(t)} = f\frac{\int_0^t C_{1e}(\tau)d\tau}{C_{1e}(t)} + v_{2p}, \quad t > t_1^*$., should hold, and a plot of $\frac{C_2(t)^*}{C_{1e}(t)_1}$ on the ordinate and $\frac{\int_0^t C_{1e}(\tau)d\tau}{C_{1t}(t)}$ on the abscissa will yield a straight line with a slope of specific flow [ml/(ml min)].

Note that this result pertains to specific flow normalized to the volume of Compartment 2. Since the size of Compartment 2 varies across animals, another measure of transfer between the two compartments must be adopted in order to make comparisons. The total flow to Compartment 2 is fV_2, through a boundary of N_{2b} voxels, where V_2 is the volume of the second compartment and N_{2b} is the number of voxels in the inner boundary of Compartment 2, i.e. the number of voxels in the thin outer rim. The volume of the second compartment is $V_2 = N_{2v}V_v$, where N_{2v} is the number of voxels in Compartment 2, and V_v is the volume of each voxel. Thus, if A_{2b} is the area of the inner surface of the outer ring ROI, a statistic that measures flux through the boundary can be calculated as $f\frac{N_{2v}V_v}{N_{2b}A_{2b}}$, in [mm^3/(mm^2 min)]. This measure is reported as the flux across the boundary of the tumor.

Since the porosity of the thin outer rim can be estimated, another interesting measure that can be generated is the mean interstitial velocity of the tumor exudate. Given a measure of flux, ϕ, the velocity of the tumor exudate in the interstitium is $\frac{\phi}{v_e}$.

We now turn to an evaluation of the errors introduced by ignoring the plasma concentration of CA in Compartment 1. From Equations [5] and [8],

$$C_2(t) = \frac{f}{v_{1e}}\int_0^t \left[C_1(\tau) - v_{1p}C_{1p}(\tau)\right]d\tau + v_{2p}C_{2p}(t)$$

$$C_2(t) = \frac{f}{v_{1e}}\int_0^t C_1(\tau)d\tau - f\frac{v_{1p}}{v_{1e}}\int_0^t C_{1p}(\tau)d\tau + v_{2p}C_{2p}(t).$$

Dividing both sides by $C_{2p}(t)$ to generate an equation in the form of the Patlak graphical equation:

$$\frac{C_2(t)}{C_{2p}(t)} = \frac{f}{v_{1e}}\frac{\int_0^t C_1(\tau)d\tau}{C_{2p}(t)} - f\frac{v_{1p}}{v_{1e}}\frac{\int_0^t C_{1p}(\tau)d\tau}{C_{2p}(t)} + v_{2p}$$

$$\frac{C_2(t)}{C_{2p}(t)} = f\frac{\int_0^t \frac{C_1(\tau)d\tau}{v_{1e}}}{C_{2p}(t)} - f\frac{v_{1p}}{v_{1e}}\frac{\int_0^t C_{1p}(\tau)d\tau}{C_{2p}(t)} + v_{2p}$$

$$\frac{C_2(t)}{C_{2p}(t)} = f\frac{\int_0^t \alpha C_1(\tau)d\tau}{C_{2p}(t)} - f\frac{v_{1p}}{v_{1e}}\frac{\int_0^t C_{1p}(\tau)d\tau}{C_{2p}(t)} + v_{2p}.$$

At equilibrium in Compartment 1, $C_{1p}(t) = \alpha C_1(t)$ and $C_{1p}(t) = C_{2p}(t)$, $t > t_1^*$

$$\frac{C_2(t)}{C_{2p}(t)} = f\left(1 - \frac{v_{1p}}{v_{1e}}\right)\frac{\int_0^t C_{1p}(\tau)d\tau}{C_{2p}(t)} + v_{2p}.$$

Thus, the bias (overestimate) introduced into the estimate of flow from Compartment 1 to Compartment 2 is of the order of the ratio of the plasma to interstitial volume in Compartment

1. In our example, this estimation error is about 10%. We note that the estimate produced by fitting the Patlak plot of Case 2 can be multiplied by $\frac{v_{1e} - v_{1p}}{v_{1e}}$, thus producing an unbiased estimate of flow. However, this would add the errors in estimating v_{1p} and v_{1e} to the errors of estimating flow between the compartments. We have judged that a known bias of around 10% is acceptable for a stable estimate of intercompartmental flow.